The effect of structural dimensionality on carrier mobility in lead-halide perovskites

The Effect of Structural Dimensionality on Carrier Mobility in Lead-Halide Perovskites

Noor Titan Putri Hartono,[1] Shijing Sun,[1] María C. Gélvez-Rueda,[2] Polly J. Pierone,[3] Matthew P. Erodici,[3] Jason Yoo,[1] Fengxia Wei,[4] Moungi Bawendi,[1] Ferdinand C. Grozema,[2] Meng-ju Sher,[3] Tonio Buonassisi,[1] and Juan-Pablo Correa-Baena[1]**

Affiliations:

[1]Massachusetts Institute of Technology, 77 Massachusetts Avenue, Cambridge, MA 02139
[2]Delft University of Technology, van der Maasweg 9, 2629 HZ Delft, The Netherlands
[3]Wesleyan University, 265 Church Street, Middletown, CT 06459
[4]Institute of Materials Research and Engineering, A*STAR, 2 Fusionopolis Way, Innovis, Singapore, 138634

Keywords: perovskite solar cells, 3D/2D perovskites, low dimensional perovskites, mobility, structural dimensionality.

Abstract:
Methylammonium lead iodide (MAPI) is a prototypical photo absorber in perovskite solar cells (PSCs), reaching efficiencies above 20%. However, its hygroscopic nature has prompted the quest to find water-resistant alternatives. Recent studies have suggested that mixing MAPI with lower dimensional, bulky-*A*-site-cation perovskites helps mitigate this environmental instability. On the other hand, low dimensional perovskites suffer from poor device performance, which has been suggested to be due to limited out-of-plane charge carrier mobility resulting from structural dimensionality and large binding energy of the charge carriers. To understand the effects of dimensionality on performance, we systematically mixed MA-based 3D perovskites with larger *A*-site cation, dimethylammonium, iso-propylammonium, and t-butylammonium lead iodide perovskites. During the shift from MAPI to lower dimensional (LD) PSCs, the efficiency is significantly reduced by 2 orders of magnitude, with short-circuit currents decreasing from above 20 mA/cm^2 to less than 1 mA/cm^2. In order to explain these decrease in performance, we studied the charge carrier mobilities of these materials using optical-pump/ terahertz-probe, time-resolved microwave photoconductivity, and photoluminescence measurements. The results show that as we add more of the low dimensional perovskites, the mobility decreases by a factor of 20 when it reaches pure LD perovskites. In addition, the photoluminescence decay fitting is slightly slower for the mixed perovskites, suggesting some improvement in the recombination dynamics. These findings indicate that changes in structural dimensionality by mixing *A*-site cations play an important role in measured charge carrier mobility, and in the performance of perovskite solar cells.

Introduction

Organic lead halide perovskites solar cells (PSCs) have reached high efficiencies in just 9 years, with a current record efficiency of 24.2%.[1,2] However, PSCs still face challenges towards commercialization, such as environmental stability. The most widely studied perovskite methylammonium lead iodide (MAPI), decomposes readily into lower dimensional perovskite structures at standard temperature and pressure, and in some cases where oxygen, ultraviolet radiation, and moisture are present, the methylammonium iodide can degrade further.[3] Mixing MAPI perovskites with bulkier *A*-site cations, such as $(PEA)_2(MA)_2[Pb_3I_{10}]$, where PEA is phenethylammonium and MA is methylammonium, forming layered structures (or lower dimensional, LD) instead of 3-dimensional (3D) structure in MAPI, can improve the long-term stability of the PSCs.[4] However, these layered perovskite structures exhibit lower device performance in comparison to their 3D analogues.[4–6] A recent study investigating the effects of LD perovskites on solar cell performance suggests that the LD perovskites with a layered structure have a strong preferred in-plane orientation due to air-liquid interface nucleation.[7] This suggests that most charge transport occurs in the in-plane instead of the out-of-plane direction, which is unfavorable for charge extraction in solar cells. In addition, the interplay between the perovskite dimensionality and its solar cell performance is not well understood.

Important parameters which determine solar cell performance are the charge carrier diffusion coefficient (D) and lifetime (τ). The carrier lifetime of various halide perovskites, both lead-based and lead-free, is relatively long, and exceeds hundreds of nanoseconds.[8–11] On the other hand, the diffusion coefficient, which linearly depends on the charge-carrier mobility, is still not well understood for LD perovskites. Hence, a deeper look at the charge-carrier mobility of LD perovskites will give a more complete picture of diffusion length, and its relationship with solar cell performance. This understanding will serve as an initial proxy for the interplay between device performance and structural dimensionality.

In this study, we intentionally broke down the high-performance, 3D-based perovskite devices by systematically mixing 3D perovskites (methylammonium lead iodide, MAPI) with LD ones, which allowed us to investigate the fundamental mechanism behind performance reduction incrementally. Three bulky *A*-site cations were used to impose structural changes within the lattice: dimethylammonium, iso-propylammonium, and t-butylammonium. Based on pre-defined

precursor volume ratios of MAPI and the LD APbI$_3$, the MAPI 3D structure with octahedron corner-sharing was forced to split into single-chained edge-sharing and corner-sharing (1D) perovskites. Solar cell performance was dramatically affected. In addition to efficiency (PCE), short-circuit current density (J_{SC}), and open-circuit voltage (V_{OC}), we also calculated W_{OC} (bandgap-voltage offset at open-circuit condition) and ΔJ_{SC}^{norm} (short-circuit current density deficit normalized) using the following Equation 1 and 2;

$$W_{OC} = \frac{E_g}{e} - V_{OC} \quad (1)$$

$$\Delta J_{SC}^{norm} = \frac{\Delta J_{SC}^{max} - J_{SC}}{\Delta J_{SC}^{max}}, \text{ where } \Delta J_{SC}^{max} = \frac{PA\lambda}{h\frac{c}{\lambda}} e(1-R) \quad (2)$$

where E_g is the bandgap, e is elementary charge, V_{OC} is open-circuit voltage, P is spectral irradiance, A is the device area, λ is the wavelength corresponding to the bandgap energy, h is Planck's constant, c is the speed of light in vacuum, and R is the reflectance. We found that PCE (power conversion efficiency) decreased by two orders of magnitude, and that W_{OC} and ΔJ_{SC}^{norm} increased by 3 and 1.8 times correspondingly, as we increased the amount of LD perovskite. The charge mobilities of these thin films were investigated using optical-pump/terahertz-probe (THz) and time-resolved microwave photoconductivity (TRMC) methods. The mobility decreased as more LD perovskites, such as t-butylammonium lead iodide (tBAPI), were added into MAPI.

Result and Discussion

Crystallographic information

Methylammonium lead iodide ($CH_3NH_3PbI_3$, MAPI, or M) with known 3D cubic structure,[12] was mixed in different volume-based ratios with layered or single-chain perovskites: dimethylammonium lead iodide ($((CH_3)_2NH)_2PbI_4$, DMAPI, or D), iso-propylammonium lead iodide ($((CH_3)_2CHNH_3)_3PbI_5$, iPAPI, or I), or t-butylammonium lead iodide ($((CH_3)_3CNH_3)_2PbI_4$, tBAPI, or T). The D, I, and T bulky A-site cations were chosen specifically due to their gradual change in ionic radii, which affects the tolerance factor and the dimensionality of the perovskite structure. The Goldschmidt's tolerance factor is an empirical unit used to describe the 3D perovskite structure based on the ionic radii of the A-site cation, the B-site cation, and/or the X-site anion. The adequate range for 3D perovskites is 0.8 to 1.0. as shown on Equation 3,[13–15]

$$t = \frac{(r_A + r_X)}{\sqrt{2}(r_B + r_X)}. \quad (3)$$

The tolerance factors of D, I, and T are obtained from Equation 3, using the effective radii for the *A*-site cations (dimethylammonium = 2.72 Å, iso-propylammonium = 3.17 Å, and t-butylammonium = 4.94 Å), the *B*-site cation (Pb^{+2} = 1.19Å), and *X*-anion (I^- = 2.2 Å).[13–15] A tolerance factor of 1.03 was found for D, 1.12 for I, and 1.49 for T, as shown on Figure 1A, in contrast to M, which has a tolerance factor of 0.91. As a comparison, the common LD used, n-butylammonium lead iodide, has a tolerance factor of 1.001.[16] In this study, to mix the perovskites, the precursor solutions of two different types of perovskites (for instance, MAPI and tBAPI), were mixed in 3 different ratios: 75%:25%, 50%:50%, and 25%:75%. Thin films were prepared following standard approaches.[17] The perovskite film was made with excess of PbI_2 (*A*I : PbI_2 = 1:1.09 for *A*PbI_3) as this strategy has been shown to yield improved solar cell performance.[18,19]

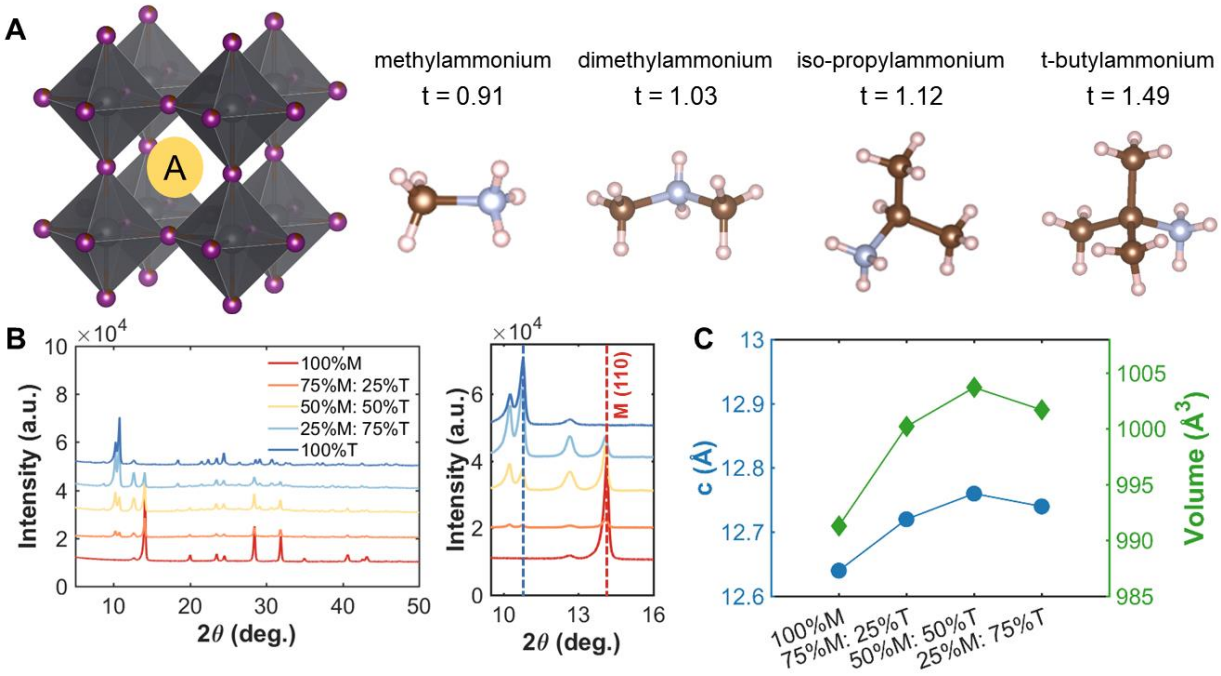

Figure 1. Crystallographic features of the perovskites studied. A. Various *A*-site cations (M, D, I, and T) with their tolerance factors. The single crystal structures for D, I, and T are shown in supporting information Figure S1. **B.** The peak shift shown on M-T series in the thin-film form. As more T was added into the film, the peak of LD perovskite became more evident. **C.** For the

thin films, the lattice parameter (*c* and volume) expanded as more T was added into M, indicating that the large *A*-site cation did get incorporated into the lattice.

To understand the effects of mixing on the structural properties, we prepared thin films with series of different ratios of MAPI to LD perovskites: MAPI-DMAPI (M-D), MAPI-iPAPI (M-I), and MAPI-tBAPI (M-T) series. We performed X-Ray Diffraction (XRD) on these thin films. The results were then refined using Pawley refinement, and the lattice parameters of the phases were obtained. Figure 1B shows how the addition of T affects the XRD patterns. One signature peak of the 100% M is located at 14.1°. As more T was added to M perovskites, the intensity of the 14.1° peak decreased, and another peak emerged at 10.8°, suggesting that a secondary phase of LD material formed within the polycrystalline thin film. To quantify how the lattice parameter of M expand with this mixing, we performed Pawley refinement of the M-T series. The lattice parameters, lattice constant and cell volume, are shown in Figure 1C. As more T was added to the M perovskite, the lattice constants expanded, suggesting that the larger *A*-site cation has an effect on the structural features of the M perovskite, in addition to the secondary phase formed. Similar trends of lattice parameter expansion were observed for the M-D and M-I series, and the data is provided on supporting information, Figure S3.

Optical properties

The 3D/LD hybrid perovskite thin films deposited on glass (M-D, M-I, and M-T) are shown in Figure 2A. A gradual change of the film colors, ranging from dark to light yellow, was observed. On the other hand, mixing LD with other LD hybrid perovskites (D-I, D-T, and I-T) yielded no visible changes.

To understand the changes in optical absorption of these mixed perovskites, UV/Vis spectroscopy was performed from 840 nm to 400 nm (Figure 2B) in thin films. As we mixed M with T, the presence of two onsets appeared, one at 825 nm (100% M absorption onset) and another at 525 nm (100% T absorption onset). Both 100% D and 100% I absorption profiles had similar onsets to 100% T, as shown in supporting information Figure S4. Tauc plot fitting was then performed to estimate the band gap for these films (fits can be found in the supporting information Figure S5). A non-linear increase in direct bandgap estimation was observed as the perovskites were mixed from 3D to LD for both absorption onsets. Additionally, the steady-state photoluminescence data

for M-T series in supporting information Figure S6 showed the slight emission shift in first absorption onset (825 nm). The bandgaps were estimated as 1.57 eV for M, 2.39 eV for D, 2.35 eV for I, and 2.34 eV for T, as shown in Figure 2C.

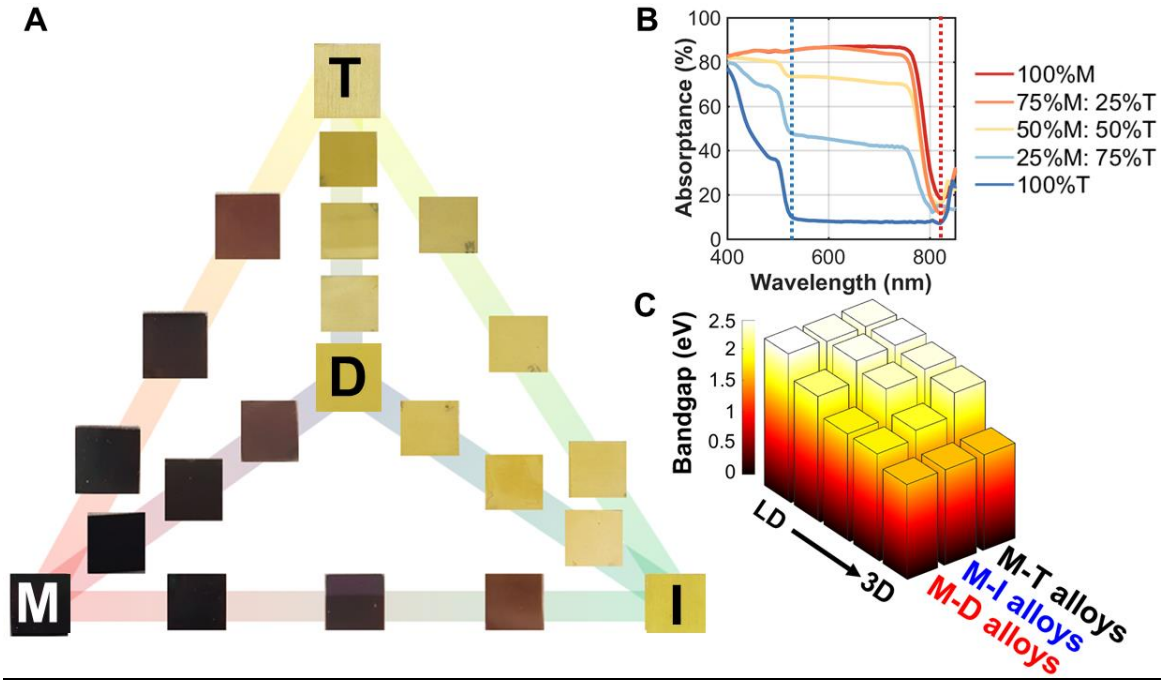

Figure 2. Optical properties of the 3D/low dimensional perovskites studied here. A. Thin films of methylammonium lead iodide (M) mixed with dimethylammonium lead iodide (D), iso-propylammonium lead iodide (I), and t-butylammonium lead iodide (T) with a set ratios: 100% : 0%, 75% : 25%, 50% : 50%, 25% : 75%, and 0% : 100%. The 100% of the M, D, I, and T films are shown on the films with corresponding letters. **B.** Absorptance of M-T series, where two absorption onsets are shown at 525 and 825 nm. **C.** The direct bandgap estimated by Tauc plots for the M-D, M-I, and M-T series at 525 nm onset; a secondary phase bandgap estimation resulting from the 825 nm onset is shown in supporting information Figure S7.

Device performance

To understand how mixing 3D with LD perovskites affects the device performance, we fabricated 120 devices for all M-D, M-I, and M-T series, and we measured the solar cells performance under solar simulator of AM1.5G at 1.0 sun operating condition. The best solar cell J-V (current density-voltage) curve data from this measurement is provided in the supporting information, Figure S8, and the complete device performance results is shown in the supporting information Table S1. We

expect that as we shift from 3D PSCs to LD PSCs, solar cell performance will be affected due to reduction in structural dimensionality. Solar cells were prepared as shown in the schematic and SEM images in Figure 3A. A fluorine-doped tin oxide (FTO) glass was used as the transparent conducting oxide, followed by the electron selective TiO_2 compact and mesoporous layers, and the hole transport Spiro-OMeTAD layer, followed by a gold layer deposited from thermal evaporation as the top electrode. The top-down scanning electron microscopy (SEM) images for the M-T series can also be seen in supporting information, Figure S9.

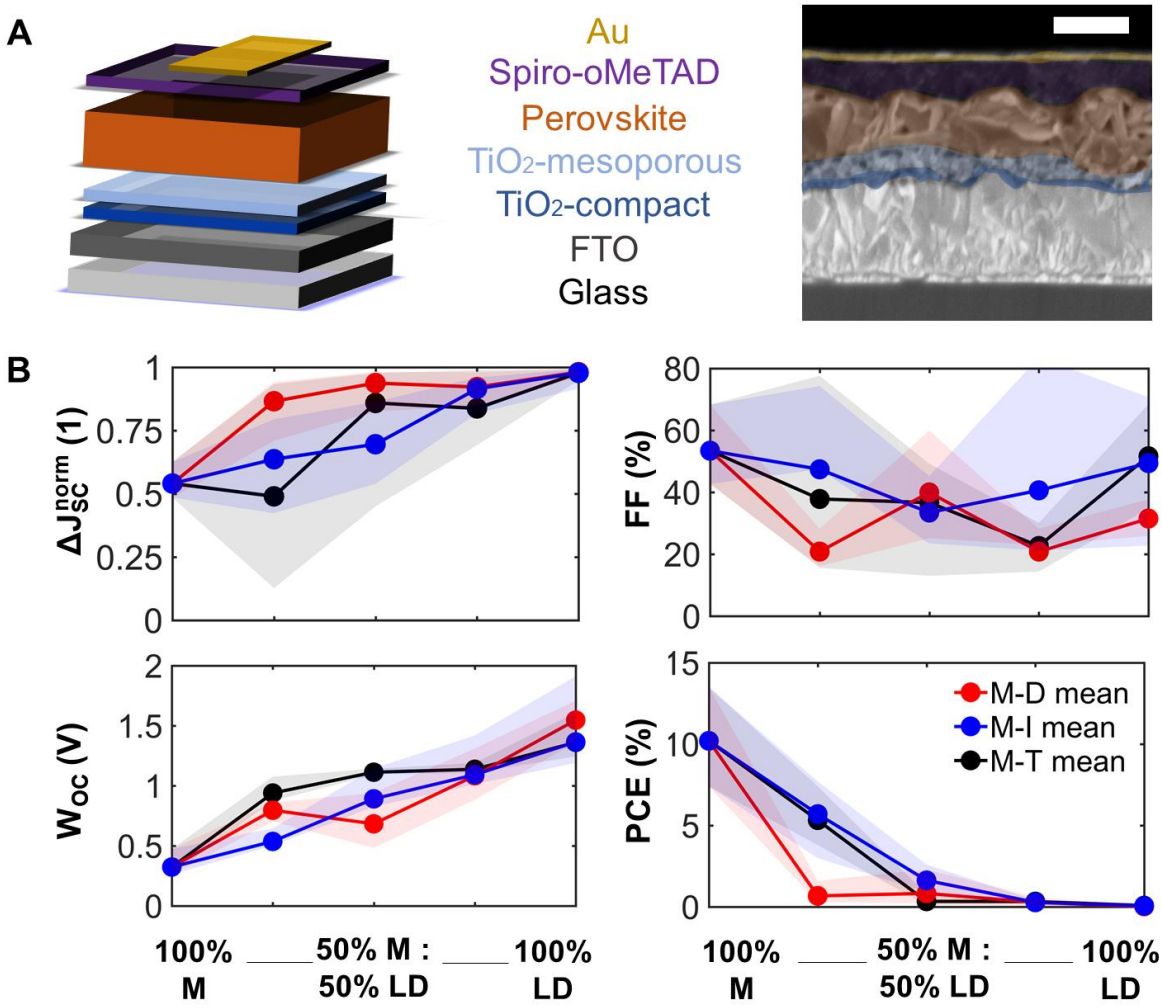

Figure 3. Solar cell performance parameters of the 3D/LD mixed perovskites. A. A schematic and a SEM image for the device stack of 25% M : 75% T device, 500 nm scale bar. **B.** Scatter plot, and average of solar cell performance metrics for M-D, M-I, and M-T series, including ΔJ_{SC}^{norm} (short-circuit current density deficit normalized), calculated by normalizing the difference between

the theoretical maximum bandgap-specific J_{SC} with the measured J_{SC}, W_{OC} (bandgap-voltage offset at open-circuit condition), calculated by subtracting the Shockley-Queisser limit, bandgap-specific V_{OC} with the measured V_{OC}, FF (fill factor), and PCE (power conversion efficiency).

Solar cell performance parameters are shown in Figure 3B, including ΔJ_{SC}^{norm} (short-circuit current density deficit normalized), FF (fill factor), W_{OC} (bandgap-voltage offset at open-circuit condition), and PCE (power conversion efficiency). W_{OC} is the difference between the Shockley-Queisser limit V_{OC} for specific bandgap at AM1.5G and the actual device V_{OC}. The W_{OC} shown in Figure 3B is based on 525 nm absorptance onset, and the W_{OC} based on 825 nm onset is shown in the supporting information Figure S10. All solar cells experienced a decrease in *Jsc* as the bulky *A*-site cations (D, I, and T) were mixed with MAPI. For example, the J_{SC} for 100% M was measured to be 16-20 mA/cm^2, decreasing to 0.1-0.5 mA/cm^2 for 100% T, a 1-2 order of magnitude reduction, which corresponds to 1.8 times increase in ΔJ_{SC}^{norm}. The W_{OC} increased by 4.2 times as we shifted from 3D (M) to 1D (D, I, and T) perovskites. No major changes in FF were found as a function of mixing. Both increase in ΔJ_{SC}^{norm} and W_{OC} led to a large drop in solar cell efficiency across all the series.

Even at relatively low concentrations of LD, e.g. 75% M and 25% of the LD perovskites, the efficiency dropped dramatically. This can be related to the changes seen in XRD data (Figure 1B), where as little as 25% of the LD perovskite yield phase segregation. A study has suggested that there is an optimum PCE for Ruddlesden-Popper perovskite solar cell devices, with a low *n*, indicating the number of 3D perovskite layers sandwiched between LD perovskites.[20] There is a possibility that the optimum device performance can be reached at a concentration of LD perovskite lower than 25%, which is not captured in Figure 4B. The introduction of secondary phases of LD characteristics can also induce changes in how charge carriers move across the thin film. Mobility of charge carriers is directly proportional to the diffusion length of the perovskite material. We studied the charge carrier mobility using optical-pump/ terahertz-probe (THz) method and time-resolved microwave photoconductivity (TRMC). According to our results, 100% T has the highest mobility among the 100% LD perovskites in this study, and gives the highest signal-to-noise ratio in both THz and TRMC measurements. Hence, we decided to focus on the mobility study on T-series to understand the effect of large cations on charge transport. We can

also infer that the mobility and structural dimensionality are independent of the size of *A*-site cation for tolerance factor above 1.00.

Charge carrier mobility

To understand the mobility of the 3D/LD hybrid perovskites we measured the time-resolved microwave photo-conductivity (TRMC) of the thin film series, similar to those for devices, on quartz glass. In these measurements, microwaves were used to probe the laser-induced change in conductance of the material, ΔG, as a function of time.[21] A typical result is shown on Figure 4A for a selected mixture 75% M: 25% T. The photoconductance, ΔG, increased during the pulse as charge carriers were created. After the excitation pulse, as the charge carriers recombined or become trapped, a decay in the ΔG was observed. From this measurement, we obtained the product of the yield of free charge carriers and sum of mobility, $\varphi \sum \mu$, from the change in photoconductance, ΔG, according to Equation 4,[21,22]

$$\varphi\,(t) \sum \mu\ = \frac{\Delta G\,(t)}{I_o \beta e F_A}; \tag{4}$$

where I_o is the the laser intensity, β corresponds to the sample geometry relating the electric field vector of the microwaves, E_{mic}, and the length of the sample in the direction of E_{mic}, e is the electronic charge, and F_A is the optical attenuation or the fraction of light absorbed at excitation wavelength. The 3D/LD hybrid perovskites were photo-excited (λ = 720 nm for 100% M, 75% M: 25% T, 50%M: 50% T, 25% M: 75% T, and λ = 490 nm for 100% T, 100% D, and 100% I) varying the photon intensity, I_o, from ~10^9 to 10^{13} photons/cm^2 (which correspond to ~ 10^{13} to 10^{17} carriers/cm^3 for a thickness of ~400 nm).[22] These intensities were in the range of standard 1.5 AM solar illumination.[23] We determined the mobility of the charge carriers from the maximum change in photoconductance, ΔG_{max}, as in this condition the decay kinetics were not dominated by trapping or second order recombination. In 75% M: 25% T and 3D/LD hybrid perovskites, ΔG_{max} was observed at intensities < ~10^{10} photons/cm^2 (which correspond to ~ 10^{14} carriers/cm^3 for a thickness of ~400 nm),[22] as shown in Figure 4A. The intensity dependent measurements and half-lifetimes from TRMC measurement for all materials are shown in the supporting information, Figure S11-S14.

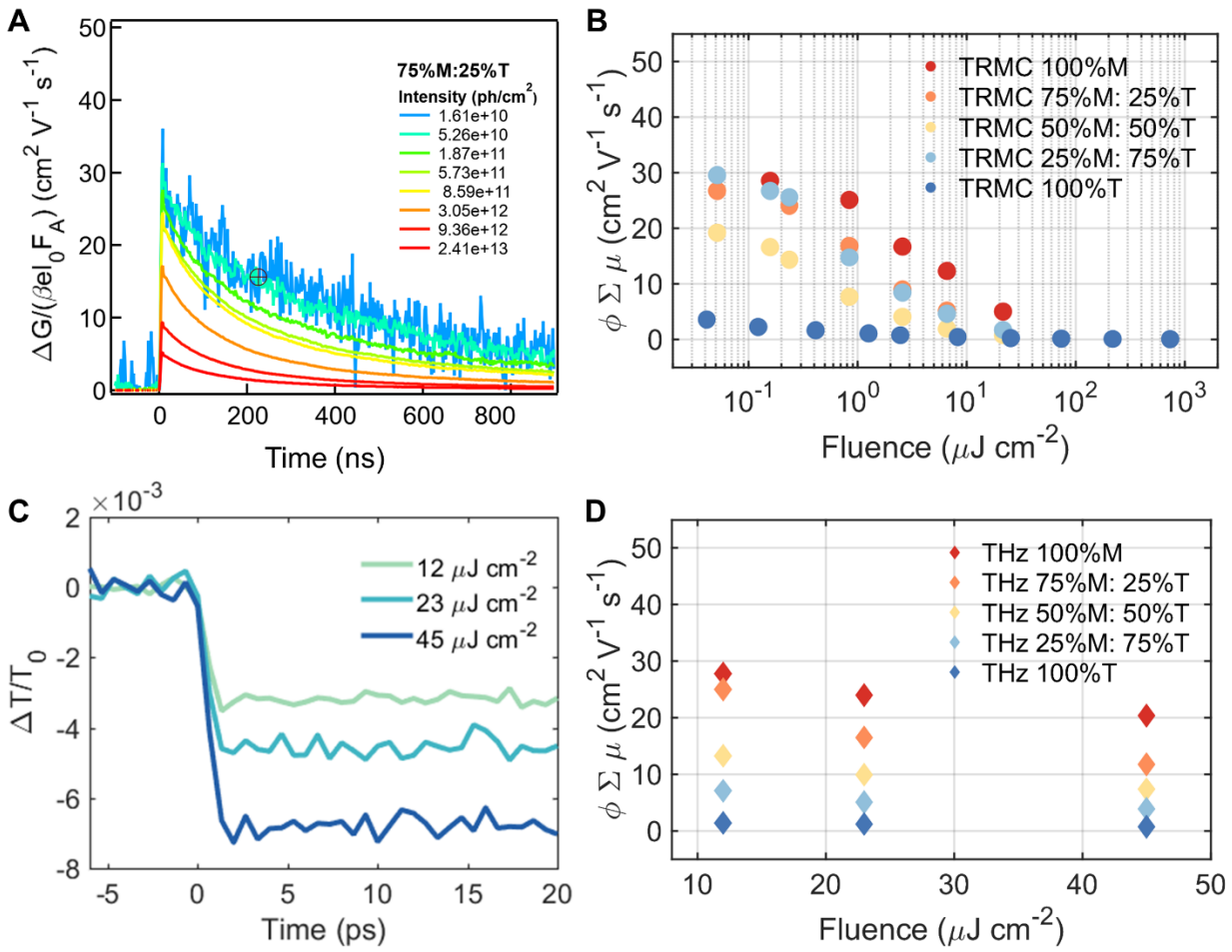

Figure 4. Probing mobilities of mixed perovskites. A. The change of photo-conductivity in TRMC as a function of time for 75% M: 25% T, excited at 720 nm (excitonic peak) for different intensities. **B.** The product of TRMC mobility and yield dissociation of free charges as a function of fluences for the M-T series excited at different wavelengths (490 nm for 100% T and 720 nm for all other series). **C.** The $\Delta T/T_0$ across 75% M: 25% T measured on optical-pump/ terahertz-probe (THz) under the different fluences, 12, 23, and 45 μJ cm^{-2}. **D.** The product of THz mobility and yield dissociation of free charges as a function of fluences (12, 23, and 45 μJ cm^{-2}) for the M-T series.

Different photoexcitation densities/ fluences affected the photoconductivity observed on the M-T series, as shown on Figure 4B. As the photoexcitation densities were increased, the effective mobilities of 100% M and the M-T series were reduced, with the exception of 25% M: 75% T. The LD sample (100% T) showed a dramatic decrease in product of mobility and yield of dissociation of charge carries with respect to the pure 3D and series, and exhibited no fluence

dependence. The low product of mobility and dissociation of charge carriers was due to strong exciton binding energy, which recombined very fast after the photoexcitation, and were unable to be captured in TRMC method. The effective mobility measured in 3D 100% M was close to 30 cm^2/Vs at fluences of around 10^{10}-10^{11}photons/cm^2, as shown in the supporting information Figure S1aA. This value is similar to values obtained for high quality films measured with the same experimental technique[22] using THz spectroscopy.[24,25] Increasing the LD content in the mixed materials yielded a drop in effective mobilities to below 30 cm^2/Vs for fluences of around 10^{10}-10^{11}photons/cm^2, as shown in figure 4B and S10B-C. Slight decreases in effective mobility have been shown to affect solar cell performance dramatically, especially in the hysteresis behavior.[26] The improvement in hysteresis behavior was also observed in our devices, across different series, as shown in supporting information Figure S15. However, we expected these large phase segregations, seen by XRD and absorption, which affected the photocurrents of the solar cell so severely, to also affect their mobilities. One hypothesis regarding the small changes detected for mobilities at low fluences is that for TRMC, we excited the 3D/LD perovskite samples at 720 nm, where most of charge carriers excited in the 3D/LD mixtures come from MAPI. This is because the phase-segregated LD perovskites absorb around 535 nm, and are not photoexcited with that particular wavelength. Therefore, only the M, 3D phase is probed.

To better understand the TRMC results, we conducted THz measurements to probe the perovskite mobilities with picosecond time scales. Transient photoconductivity measurements were performed on the same set of samples as for TRMC (the M-T series), this time excited at 400 nm to include the charge carriers excited from T, and to be able to observe the LD charge carrier mobility effects. We calculated effective carrier mobility using optical-pump, where we obtained the $\Delta T/T_0$ result as shown on Figure 4C and in supporting information Figure S16 for M-T series. Carrier mobility is calculated from the peak of the conductivity at zero pump-probe delay time. The photoconductivity was highest for the 100% M sample and the conductivity reduced with increasing percentage of T, as shown on Figure 4D. Samples with more LD characteristics showed lower mobility.[6] Similar to the TRMC result, we found that carrier mobility depended on excitation density and the lower the excitation density, the higher the effective mobility was.

The discrepancy between the TRMC and THz mobilities at the same fluences (10 to 50 $\mu J\ cm^{-2}$) can be attributed to the different time resolutions of each technique. The time resolution of TRMC

is in nanosecond regime, whereas that of THz is in the picosecond regime. Therefore, when measuring mobilities by TRMC, we tend to lose some of that initial signal from the first few hundred picoseconds, which can be collected by THz spectroscopy. Regardless of the absolute intensity, the effective mobilities' trend with respect to fluence- and composition-dependency are similar for both techniques.

Conclusions

In this study, 3D/LD hybrid perovskites solar performance and their material properties were studied. The addition of various LD perovskites (DMAPI, iPAPI, tBAPI) into MAPI showed optical, structural, and charge carrier transport property changes, which lead to change in solar device performance. We present three important findings when mixing 3D with LD perovskites: 1) most of the additions of LD perovskites result in phase segregation of LD and 3D structures within the polycrystalline films; 2) photocurrents are massively hampered by 25% or more of the LD perovskite; and 3) the phase segregation of LD perovskites leads to reduced effective mobilities in the overall thin film. Both TRMC and THz measurements have enabled us to quantify the effective charge carrier mobilities across different photoexcitation densities and timescales. Therefore, although LD perovskites can improve environmental stability, their low charge carrier effective mobility can adversely affect solar cell performance in hybrid organic/inorganic perovskites. Hence, 3D/LD perovskite mixing must be carefully controlled when developing these types of series in solar cell devices.

Experimental section

Film fabrication. For the various volume-based mixtures of 3D/LD perovskites, 4 equimolar stock solutions were prepared: methylammonium lead iodide ($MAPbI_3$, or M), dimethylammonium lead iodide ($DMAPbI_3$, or D), iso-propylammonium lead iodide ($iPAPbI_3$, or I), and t-butylammonium lead iodide ($tBAPbI_3$, or T). Initially, a 1.5 M PbI_2 (Sigma-Aldrich) solution was dissolved in 9:1 DMF: DMSO mixed solvents, before mixing them with amine powder. For every gram of MAI powder (Dyesol), DMAI powder (Dyesol), iPAI powder (Dyesol), and tBAI powder (Dyesol), we added 5.10 mL, 4.67 mL, 4.25 mL, and 3.95 mL of 1.5 M PbI_2 solution correspondingly. These 4 stock solutions were then mixed according to prescribed ratios.

65 μL of perovskite solution was then deposited on the pre-cleaned substrate (quartz for TRMC and THz measurement, glass slides for UV-Vis, XRD, steady-state PL, and TRPL measurements, and FTO with TiO_2 for device fabrication), and spincoated with the 2-step program: 1000 rpm for 10 s and acceleration of 200 rpm/s, then 6000 rpm for 30 s and acceleration of 2000 rpm/s. 5 seconds after the start of the second step, 200 μL of chlorobenzene was dropped on the substrate. Then, the deposited film was annealed on the hotplate at 100°C for 10 minutes.

Single crystal growth. *For the iso-propylammonium lead iodide (iPAPI, or I):* 0.093g iPAI and 0.23g PbI_2 (molar ratio 1:1) were fully mixed in 300 μL of hydriodic acid in 23 ml stainless steel Parr autoclave and heated at 120°C for 3 days. The crystals were then cooled and dried under ambient condition. *For the t-butylammonium lead iodide (tBAPI, or T):* 0.5 g of PbI_2 was dissolved in in 500 μL of hydriodic acid containing ≤1.5% hyposphorous acid as stabilizer, ACS reagent, ≥47.0% (Sigma-Aldrich), and heated up to about 70°C using water bath. Then, 0.24 g of t-butylammonium iodide powder from Dyesol was added into the solution while being stirred. The solution was then slowly cooled at 0.2°C/minute rate, and left in the fridge for 2 weeks, before filtered and dried under ambient air.

Solar cell fabrication. The etched FTO glass (Pilkington, TECS) substrates were cleaned using 2% Hellmanex in water, ethanol, and UV ozone. A TiO_2 compact layer solution was made by mixing the titanium diisopropoxide bis(acetylacetonate) 75% wt. (Sigma-Aldrich) in ethanol (1:10 V/V ratio, and deposited using spray pyrolysis method at 500°C. The TiO_2 mesoporous layer was prepared by mixing 1:5 W/W of TiO_2 paste (SureChem, SC-HT040): solvent mix (3.5:1 W/W of terpineol: 2-methoxy ethanol) and spincoating it using 2-step program: 500 rpm for 5 seconds, then 2500 rpm for 50 s. The substrate was then annealed at 500°C. For the hole transport layer, we used spiro-OMeTAD (2,2′7,7′-tetrakis-(N,N-di-p-methoxyphenyl amine)-9,9′-spirobifluorene, LumTec LT-S922). For every gram of spiro-OMeTAD, we used 227 μL of Li-TFSI (Sigma-Aldrich, 1.8 M in acetonitrile) solution, 394 μL of 4-tert-butylpyridine (Sigma-Aldrich) solution, 98 μL cobalt complex (FK209, Lumtec, 0.25 M tris(2-(1H-pyrazol-1-yl)-4-tertbutylpyridine) cobalt(III) tris(bis(trifluoromethylsulfonyl)imide) in acetonitrile) solution, and 10,938 μL of chlorobenzene. 65 μL of the mixed spiro solution was deposited and spincoated at 3000 rpm for 30 s. Finally, a 100 nm gold top electrode was deposited by thermal evaporation, with an active area of 0.16 cm^2.

General characterization. The transmission and reflection for the thin film was measured using Perkin-Elmer Lambda 950 UV/Vis Spectrophotometer (Perkin-Elmer). The method established by Tauc,[27] was then used to extract the bandgaps by assuming direct band gaps with an approximate thickness of 300 nm film. The crystal structure and phase of the films were characterized using an XRD (Rigaku SmartLab), with Cu-Kα sources. Pawley refinements of M-D, M-I, and M-T series compounds were performed using Highscore Plus and Topas. The film morphology and device cross-section were investigated by a Zeiss Supra 55VP field-emission scanning electron microscope (FESEM, Zeiss). J−V curves were measured using a solar simulator (Newport, Oriel Class AAA, 91195A) with a source meter (Keithley 2420) at 100 mW cm^{-2}, AM1.5G illumination, and a calibrated Si-reference cell certified by the NREL. The J−V curves were measured at 10 mV/s. J−V curves for all devices were measured by masking the active area with a metal mask of 0.094 cm^2.

Photo-conductivity measurements. Laser induced time-resolved microwave conductivity (TRMC) measurements were carried out on samples deposited on quartz substrates and placed in a sealed resonance cavity inside a nitrogen-filled glovebox. The TRMC technique measures the fractional change in microwave (8−9 GHz) power absorbed by the sample after pulsed excitation (repetition rate 10 Hz) of the thin films at their respective excitonic absorption peaks (~720 nm for methylammonium containing samples 100% M, 75% M : 25% T, 50% M: 50% T, 25% M: 75% T, and ~500 nm for LD D, I, and T). The time resolution of these measurements are limited by the width of the laser pulse (3.5 ns FWHM) and the response time of the microwave system (open cell ~8 ns). Before and during the photo-conductance measurements, the samples were not exposed to moisture and air to prevent degradation.[21,22]

Optical-pump/THz-probe measurements. Charge carrier mobilities at THz frequencies were obtained by optical-pump/ terahertz-probe, transient photoconductivity measurements.[28] Both the optical pump pulse and THz probe pulse were generated from the same Ti:Sapphire femtosecond laser amplifier (800 nm center wavelength, 2.0 mJ pulse energy, and 1 kHz repetition rate) with its output energy separated into three paths: optical pump path, THz probe path, and THz detection path. The optical pump pulses were frequency doubled to 400 nm using a beta barium borate (BBO) crystal and then focused to a 2-mm diameter at maximum fluence of 45 μJ cm^{-2}. The THz probe pulses (peak frequency at 1.2 THz) were generated from a two-color laser-induced gas plasma and focused to 1-mm in diameter on the sample. The arrival time differences between the

pump and the probe pulses on the sample were controlled by a delay stage. We used electro-optical sampling technique with a 1.0-mm thick <110> ZnTe crystal to detect the waveform of the THz pulse. We used lock-in techniques to record change in THz transmission ΔT relative to its initial THz transmission T_0 at the peak of the THz waveform. We calculated transient photoconductivity using $\Delta\sigma = \left(\frac{1+n_{SiO_2}}{Z_0 d}\right)\left|\frac{\Delta T}{T_0}\right|$, where $n_{SiO_2} = 2.1$ is the index of refraction of the quartz substrate at 1.2 THz, $Z_0 = 377\ \Omega$ is the impedance of free space, *d* was the depth of the excited carriers (taken to be the absorption depth). Effective carrier mobility μ was further obtained from $\Delta\sigma = q\Delta n_0\mu$, where q was elementary charge, and Δn_0 was the initial excited carrier density. The initial excited carrier density Δn_0 was taken to be ϕn_{photon}, with ϕ being the yield of photon-to-carrier generation and n_{photon} being the density of absorbed photons.

Photoluminescence measurements. Steady-state photoluminescence was recorded using a 532 nm diode laser (Thorlabs) coupled with a monochromator (Princeton Instruments, SP-300i) and a InGaAs detector (Thorlabs, DET10N). Time resolved photoluminescence lifetimes were collected using a 405 nm picosecond pulsed diode laser (Picoquant) with a repetition rate of 500kHz using a pulse generator (Stanford Research; DG535). The laser was set to average power of ~10 nW using neutral density filters and focused to a 150 μm spot on the perovskite film. The emission from the film was collected and collimated using an off-axis parabolic mirror (Thorlabs, MPD269V) and sent into a silicon single photon counting detector (Perkin-Elmer, SPCM-AQR-13). Scattered laser excitation was suppressed using a 405 nm notch filter and a 420 nm longpass filter. Photon arrival times were recorded using a time-correlated single photon counting card (Picoquant, PicoHarp 300).

Acknowledgements

NTPH, SS, TB, and JPCB are supported by the NSF grant CBET-1605495. JPCB is supported by the DOE EERE Postdoctoral Research Award. JY is funded by the Institute for Soldier Nanotechnology (ISN) grant W911NF-13-D-0001 and by the National Aeronautics and Space Administration (NASA) grant NNX16AM70H. FW is funded by the Accelerated Materials Development for Manufacturing from IMRE, A*STAR, grant number A1898b0043. M-JS, PJP, and MPE are supported by Wesleyan College of the Environment Faculty-Led Research Project

Grants. MCGR and FCG are supported by funding from the European Research Council Horizon 2020 ERC Grant Agreement no. 648433.

References

1. Correa-Baena J-P, Saliba M, Buonassisi T, et al. Promises and challenges of perovskite solar cells. *Science*. 2017;358(6364):739-744. doi:10.1126/science.aam6323

2. National Renewable Energy Laboratory. *Best Research-Cell Efficiencies*.; 2019. https://www.nrel.gov/pv/assets/pdfs/best-research-cell-efficiencies-190416.pdf. Accessed May 13, 2019.

3. Niu G, Guo X, Wang L. Review of recent progress in chemical stability of perovskite solar cells. *J Mater Chem A*. 2015;3(17):8970-8980. doi:10.1039/C4TA04994B

4. Smith IC, Hoke ET, Solis-Ibarra D, McGehee MD, Karunadasa HI. A Layered Hybrid Perovskite Solar-Cell Absorber with Enhanced Moisture Stability. *Angew Chemie Int Ed*. 2014;53(42):11232-11235. doi:10.1002/anie.201406466

5. Cao DH, Stoumpos CC, Farha OK, Hupp JT, Kanatzidis MG. 2D Homologous Perovskites as Light-Absorbing Materials for Solar Cell Applications. doi:10.1021/jacs.5b03796

6. Milot RL, Sutton RJ, Eperon GE, et al. Charge-Carrier Dynamics in 2D Hybrid Metal–Halide Perovskites. *Nano Lett*. 2016;16(11):7001-7007. doi:10.1021/acs.nanolett.6b03114

7. Chen AZ, Shiu M, Ma JH, et al. Origin of vertical orientation in two-dimensional metal halide perovskites and its effect on photovoltaic performance. *Nat Commun*. 2018;9(1):1336. doi:10.1038/s41467-018-03757-0

8. Stranks SD, Eperon GE, Grancini G, et al. Electron-hole diffusion lengths exceeding 1 micrometer in an organometal trihalide perovskite absorber. *Science*. 2013;342(6156):341-344. doi:10.1126/science.1243982

9. Slavney AH, Hu T, Lindenberg AM, Karunadasa HI. A Bismuth-Halide Double Perovskite with Long Carrier Recombination Lifetime for Photovoltaic Applications. *J Am Chem Soc*. 2016;138(7):2138-2141. doi:10.1021/jacs.5b13294

10. Correa-Baena J-P, Nienhaus L, Kurchin RC, et al. A-Site Cation in Inorganic

A<inf>3</inf>Sb<inf>2</inf>I<inf>9</inf>Perovskite Influences Structural Dimensionality, Exciton Binding Energy, and Solar Cell Performance. *Chem Mater*. 2018;30(11). doi:10.1021/acs.chemmater.8b00676

11. Brandt RE, Poindexter JR, Gorai P, et al. Searching for "Defect-Tolerant" Photovoltaic Materials: Combined Theoretical and Experimental Screening. *Chem Mater*. 2017;29(11):4667-4674. doi:10.1021/acs.chemmater.6b05496

12. Brivio F, Frost JM, Skelton JM, et al. Lattice dynamics and vibrational spectra of the orthorhombic, tetragonal, and cubic phases of methylammonium lead iodide. *Phys Rev B*. 2015;92(14):144308. doi:10.1103/PhysRevB.92.144308

13. Kieslich G, Sun S, Cheetham AK. Solid-state principles applied to organic–inorganic perovskites: new tricks for an old dog. *Chem Sci*. 2014;5(12):4712-4715. doi:10.1039/C4SC02211D

14. Becker M, Klüner T, Wark M. Formation of hybrid ABX 3 perovskite compounds for solar cell application: first-principles calculations of effective ionic radii and determination of tolerance factors. *Dalt Trans*. 2017;46(11):3500-3509. doi:10.1039/C6DT04796C

15. Hoefler SF, Trimmel G, Rath T. Progress on lead-free metal halide perovskites for photovoltaic applications: a review. *Monatshefte für Chemie - Chem Mon*. 2017;148(5):795-826. doi:10.1007/s00706-017-1933-9

16. Hsieh C-M, Yu Y-L, Chen C-P, Chuang S-C. Effects of the additives *n* -propylammonium or *n* -butylammonium iodide on the performance of perovskite solar cells. *RSC Adv*. 2017;7(88):55986-55992. doi:10.1039/C7RA11286F

17. Saliba M, Correa-Baena J-P, Wolff CM, et al. How to Make over 20% Efficient Perovskite Solar Cells in Regular (*n–i–p*) and Inverted (*p–i–n*) Architectures. *Chem Mater*. 2018;30(13):4193-4201. doi:10.1021/acs.chemmater.8b00136

18. Bi D, Tress W, Dar MI, et al. Efficient luminescent solar cells based on tailored mixed-cation perovskites. *Sci Adv*. 2016;2(1):e1501170. doi:10.1126/sciadv.1501170

19. Roldán-Carmona C, Gratia P, Zimmermann I, et al. High efficiency methylammonium lead triiodide perovskite solar cells: the relevance of non-stoichiometric precursors. *Energy Environ Sci*. 2015;8(12):3550-3556. doi:10.1039/C5EE02555A

20. Blancon J-C, Tsai H, Nie W, et al. Extremely efficient internal exciton dissociation through edge states in layered 2D perovskites. *Science*. 2017;355(6331):1288-1292. doi:10.1126/science.aal4211

21. Savenije TJ, Ferguson AJ, Kopidakis N, Rumbles G. Revealing the Dynamics of Charge Carriers in Polymer:Fullerene Blends Using Photoinduced Time-Resolved Microwave Conductivity. *J Phys Chem C*. 2013;117(46):24085-24103. doi:10.1021/jp406706u

22. Hutter EM, Eperon GE, Stranks SD, Savenije TJ. Charge Carriers in Planar and Meso-Structured Organic–Inorganic Perovskites: Mobilities, Lifetimes, and Concentrations of Trap States. *J Phys Chem Lett*. 2015;6(15):3082-3090. doi:10.1021/acs.jpclett.5b01361

23. Jiang C-S, Yang M, Zhou Y, et al. Carrier separation and transport in perovskite solar cells studied by nanometre-scale profiling of electrical potential. *Nat Commun*. 2015;6(1):8397. doi:10.1038/ncomms9397

24. Eperon GE, Burlakov VM, Docampo P, Goriely A, Snaith HJ. Morphological Control for High Performance, Solution-Processed Planar Heterojunction Perovskite Solar Cells. *Adv Funct Mater*. 2014;24(1):151-157. doi:10.1002/adfm.201302090

25. Milot RL, Eperon GE, Snaith HJ, Johnston MB, Herz LM. Temperature-Dependent Charge-Carrier Dynamics in $CH_3NH_3PbI_3$ Perovskite Thin Films. *Adv Funct Mater*. 2015;25(39):6218-6227. doi:10.1002/adfm.201502340

26. Turren-Cruz SH, Saliba M, Mayer MT, et al. Enhanced charge carrier mobility and lifetime suppress hysteresis and improve efficiency in planar perovskite solar cells. *Energy Environ Sci*. 2018;11(1):78-86. doi:10.1039/c7ee02901b

27. Tauc J. Optical properties and electronic structure of amorphous Ge and Si. *Mater Res Bull*. 1968;3(1):37-46. doi:10.1016/0025-5408(68)90023-8

28. Sher M-J, Simmons CB, Krich JJ, et al. Picosecond carrier recombination dynamics in chalcogen-hyperdoped silicon. *Appl Phys Lett*. 2014;105(5):053905. doi:10.1063/1.4892357

The Effect of Structural Dimensionality on Carrier Mobility in Lead-Halide Perovskites

Supporting Information

Affiliations:

[1]Massachusetts Institute of Technology, 77 Massachusetts Avenue, Cambridge, MA 02139
[2]Delft University of Technology, van der Maasweg 9, 2629 HZ Delft, The Netherlands
[3]Wesleyan University, 265 Church Street, Middletown, CT 06459
[4]Institute of Materials Research and Engineering, A*STAR, 2 Fusionopolis Way, Innovis, Singapore, 138634

Figure S1. The single crystal XRD results for DMAPI (dimethylammonium lead iodide/ D), iPAPI (iso-propylammonium lead iodide/ I), and tBAPI (t-butylammonium lead iodide/ T), in comparison to MAPI (methylammonium lead iodide/ M). Note that for the T, due to crystal growth process, H_2O got incorporated into the single crystal structure as shown in the figure. Thus, the single crystal structure for T is in different phase to the thin-film one shown in supporting information Figure S2.

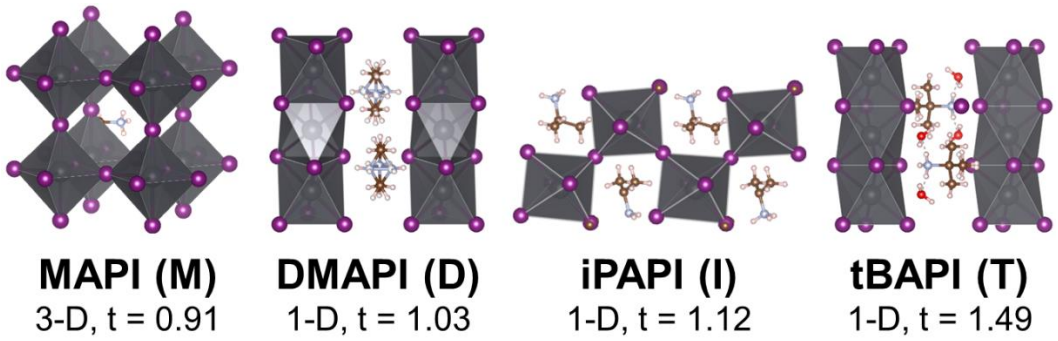

To resolve the previously unknown crystal structure of I and T, single crystals were prepared in order to perform single-crystal XRD. The I single crystal was synthesized using a hydrothermal technique,[1] and the T single crystal was made using a solution cooling technique.[2] The crystal structure of D has been previously resolved by Mancini et al. with a $P6_3/mmc$ space group.[3] The result shows that I has a space group of $P2_12_12_1$ and T has a space group $P2_1/m$, as shown on Figure 1A. Note that the T in single crystal phase is different from the T in thin film phase, since T's single crystal growth in water bath under ambient air introduced water into the structure, which can be observed in supporting information Figure S1. In the bulk, both D and T have a 1D-chain, edge-sharing structure. I, on the other hand, has a 1D-chain, corner-sharing structure. Interestingly,

the increase in size of *A*-site cation does not necessarily correspond to the decrease in structural dimensionality of the bulk material.

Figure S2. The powder XRD results for tBAPI thin film and tBAPI single crystal, indicating they have two different phases.

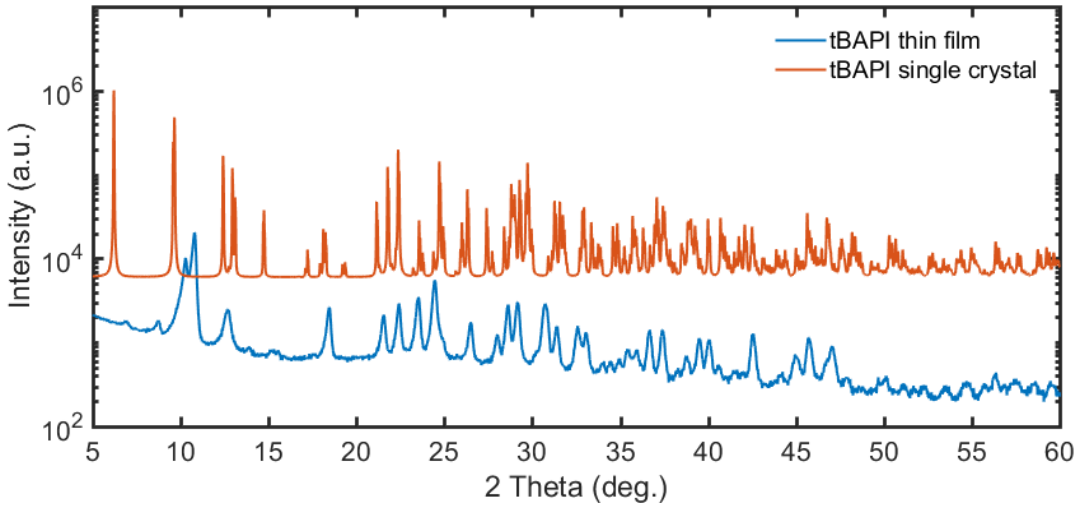

Figure S3. The lattice parameter expansion for **A.** M-D alloys, and **B.** M-I alloys.

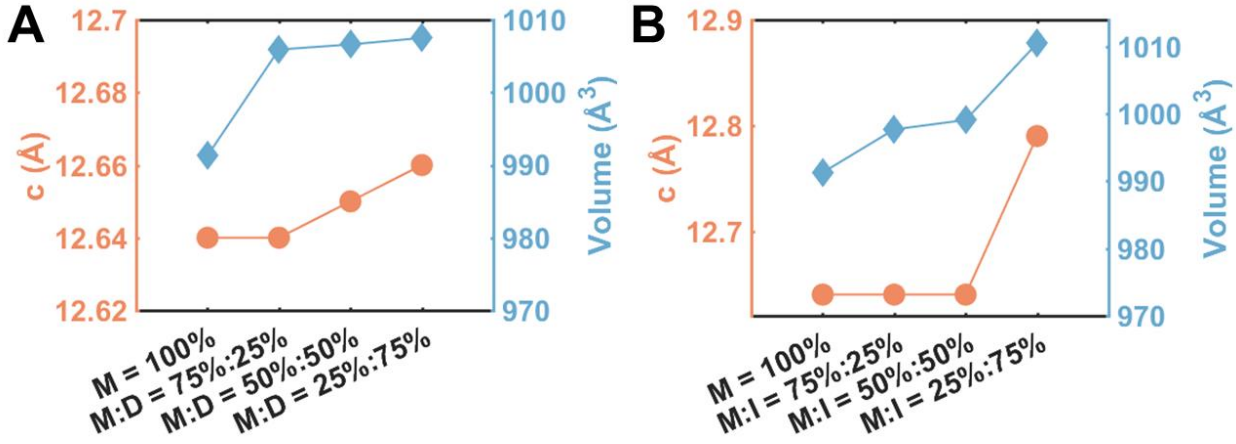

Figure S4. The absorptance of D, I, M, and T.

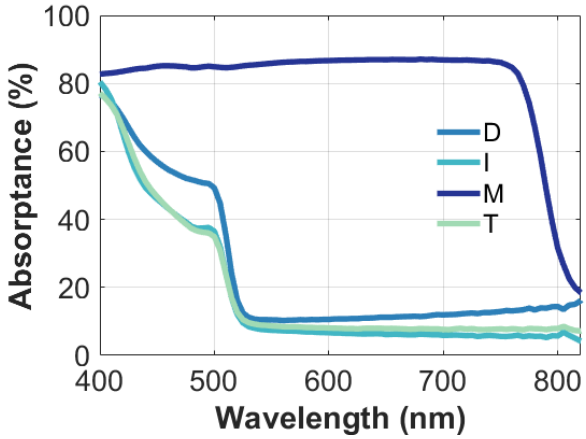

Figure S5. Direct bandgap Tauc plot fitting for both 525 nm and 825 nm absorption onsets for **A.** 100% M, **B.** 75% M: 25% T, **C.** 50% M : 50% T, **D.** 25% M : 75% T, and **E.** 100% T.

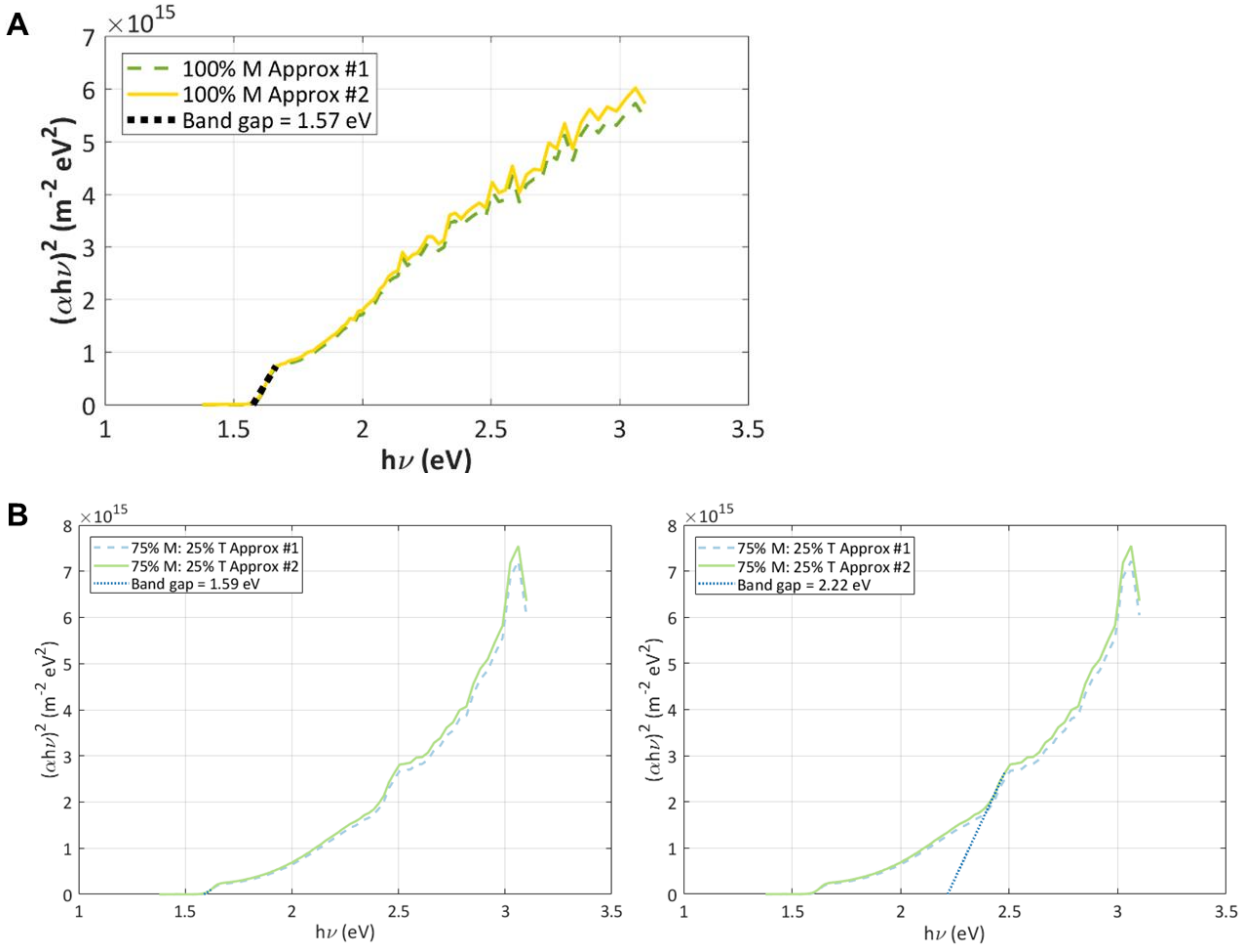

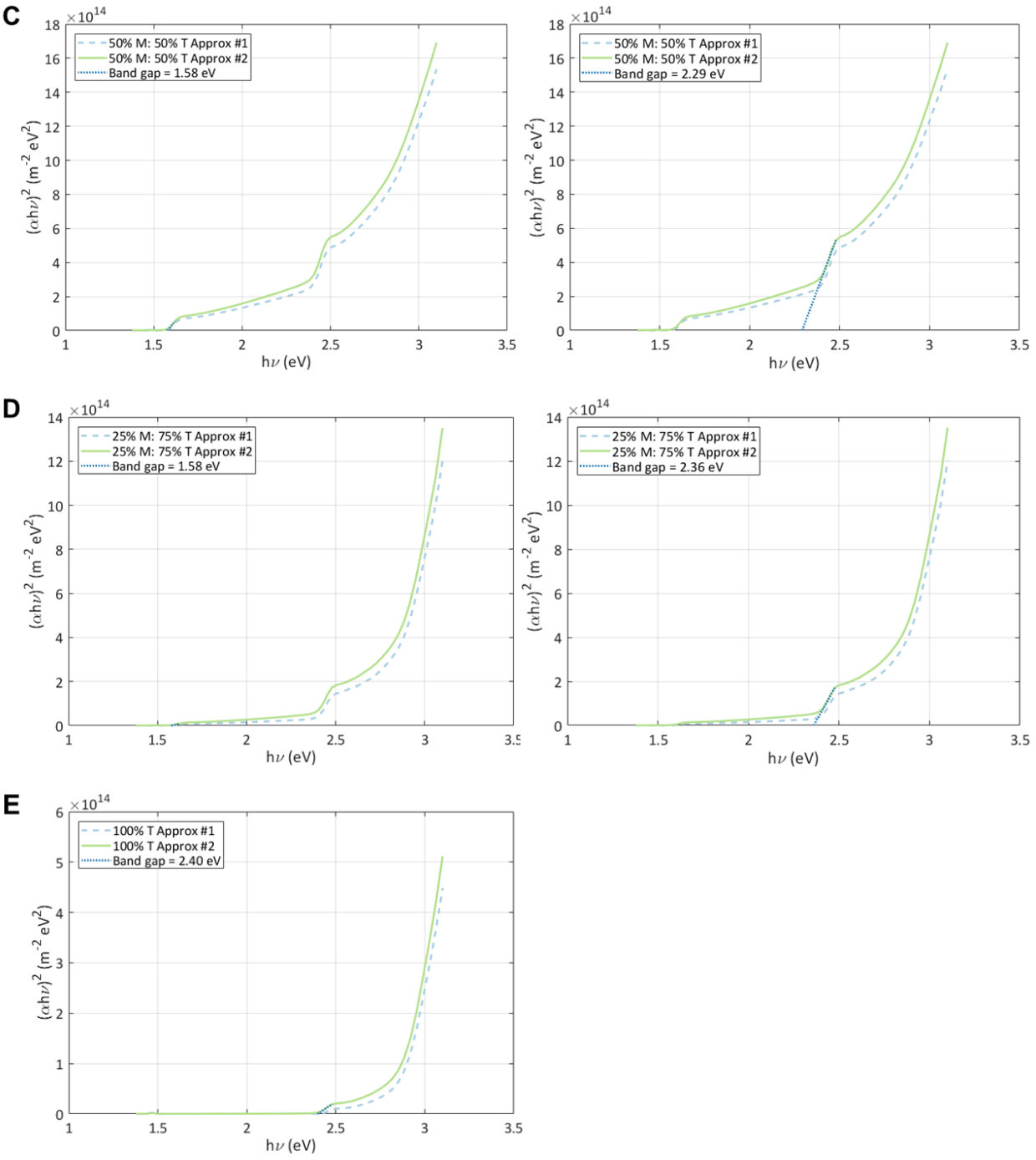

Figure S6. A. The steady-state photoluminescence result for M-T alloys, excited at 532 nm, which shows a bandgap shift towards higher energy as we add more LD perovskite. **B.** The time-resolved photoluminescence for M-T alloys. **C.** The corresponding highest lifetime based on biexponential fitting of M-T alloys PL decay.

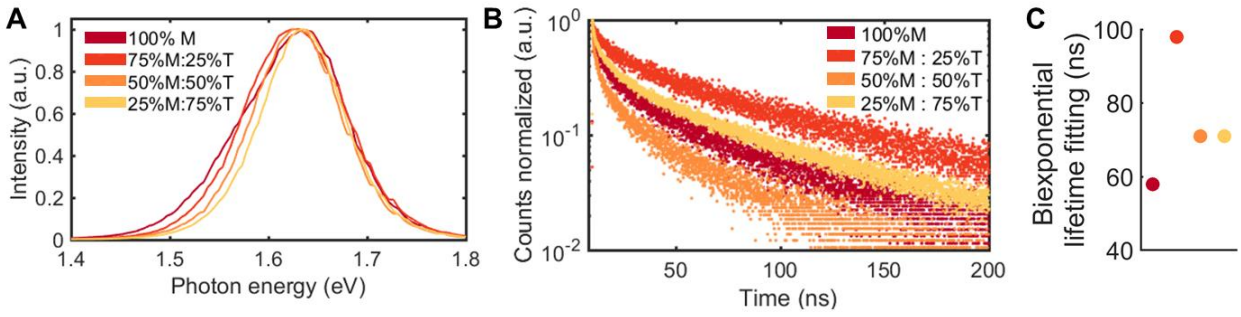

Figure S7. Tauc plot fittings for **A.** direct bandgap from 825 nm absorption onset of 3D/LD alloys, and **B.** indirect bandgap 3D/LD alloys.

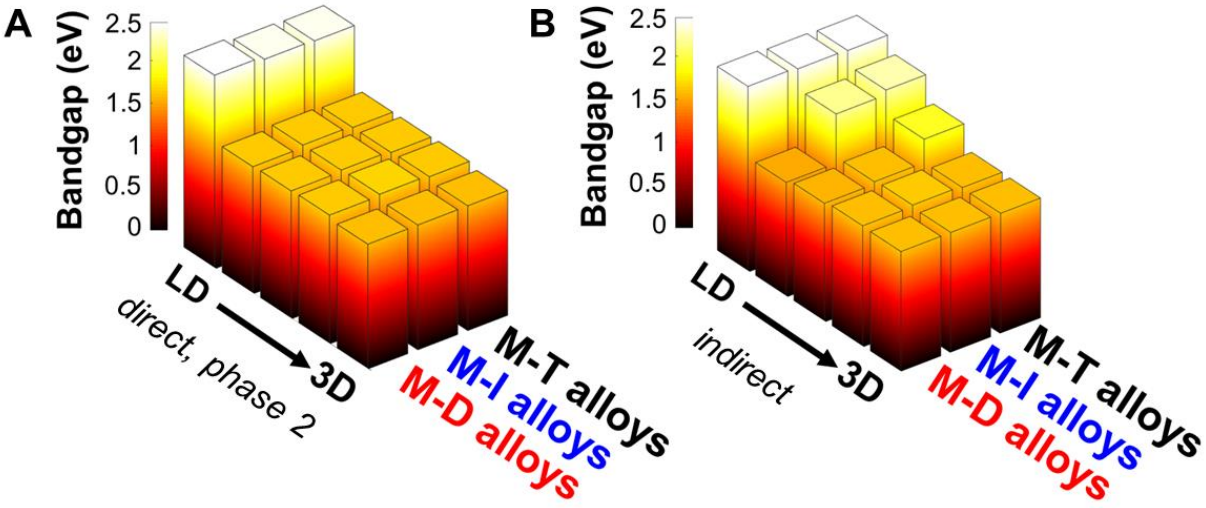

Figure S8. The best device JV curve data for M-D alloys in reverse (**A.**) and forward (**B.**) direction, M-I alloys in reverse (**C.**) and forward (**D.**) direction, and M-T alloys in reverse (**E.**) and forward (**F.**) direction . Each point at JV curve was taken with voltage settling time of 1000 ms.

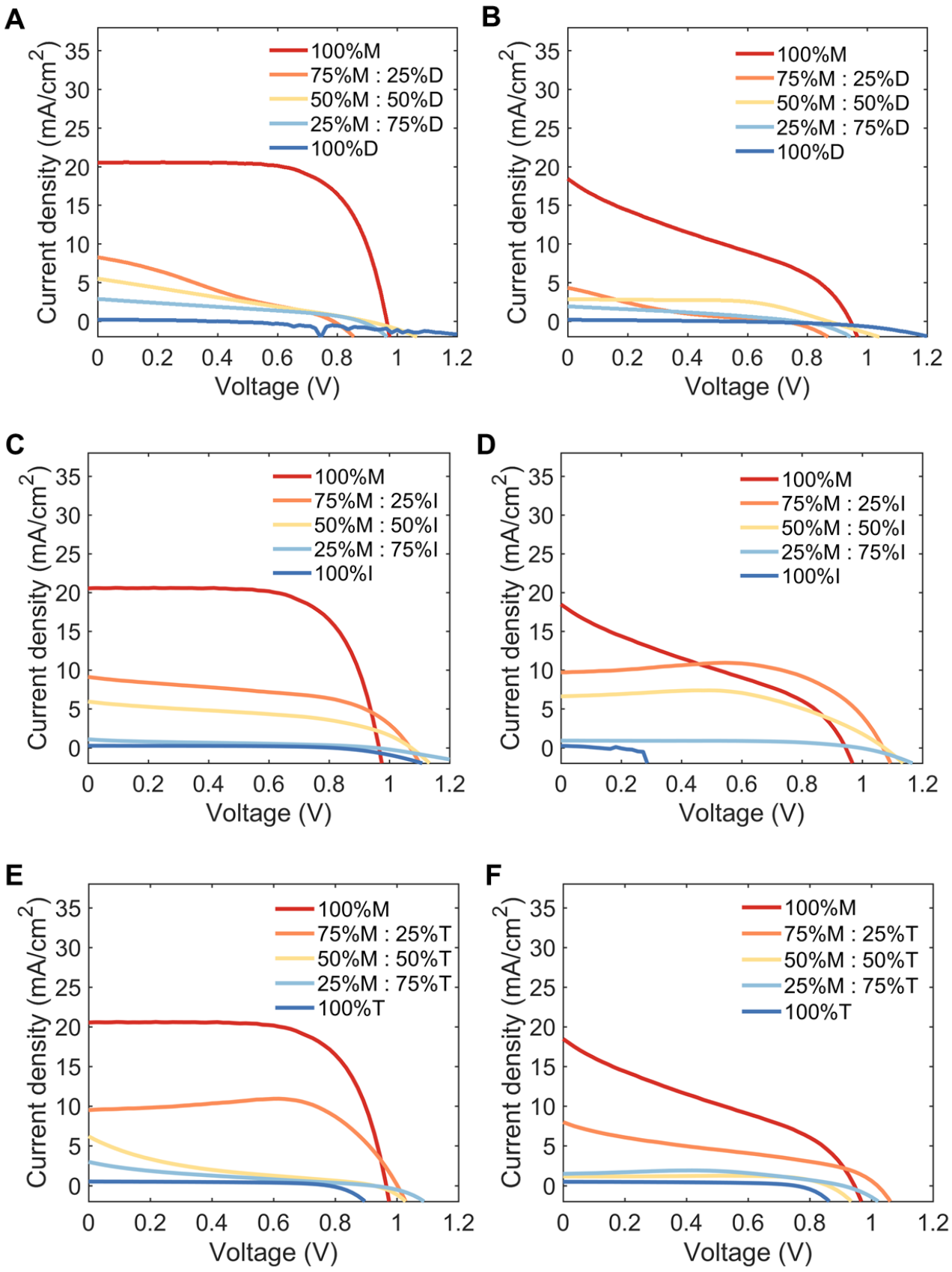
A
B
C
D
E
F
Current density (mA/cm^2)
Voltage (V)
100%M
75%M : 25%D
50%M : 50%D
25%M : 75%D
100%D
75%M : 25%I
50%M : 50%I
25%M : 75%I
100%I
75%M : 25%T
50%M : 50%T
25%M : 75%T
100%T

Table S1. The PCE, ΔJ_{SC}^{norm}, W_{OC}, and FF for all the M-D, M-I, and M-T samples.

	PCE (%)			ΔJ_{SC}^{norm} **(1)**			***Woc* (V)**			**FF (%)**		
	25th percent-ile	75th percent-ile	Mean	25th percent-ile	75th percent-ile	Mean	25th percent-ile	75th percent-ile	Mean	25th percent-ile	75th percent-ile	Mean
M-D												
100% M	9.25	11.20	10.20	0.511	0.565	0.541	0.266	0.381	0.323	45.38	61.33	53.42
75% M: 25% D	0.30	0.95	0.68	0.813	0.924	0.866	0.754	0.848	0.780	17.60	23.45	20.83
50% M: 50% D	0.25	1.18	0.83	0.922	0.972	0.938	0.564	0.791	0.683	28.65	51.80	39.94
25% M: 75% D	0.10	0.55	0.27	0.870	0.977	0.922	0.933	1.288	1.083	24.55	23.45	20.83
100% D	0.00	0.03	0.02	0.975	0.988	0.981	1.406	1.662	1.547	28.6	34.73	31.50
M-I												
100% M	9.25	11.20	10.20	0.511	0.565	0.541	0.266	0.381	0.323	45.38	61.33	53.42
75% M: 25% I	4.75	6.60	5.70	0.566	0.700	0.637	0.504	0.560	0.537	49.43	66.93	47.41
50% M: 50% I	1.40	1.95	1.63	0.582	0.801	0.696	0.840	0.903	0.891	27.10	39.20	33.45
25% M: 75% I	0.20	0.30	0.28	0.906	0.941	0.915	1.040	1.080	1.092	32.23	44.45	40.63
100% I	0.03	0.10	0.06	0.975	0.989	0.979	1.243	1.367	1.365	44.68	56.28	49.39
M-T												
100% M	9.25	11.20	10.20	0.511	0.565	0.541	0.266	0.381	0.323	45.38	61.33	53.42
75% M: 25% T	4.00	7.25	5.33	0.286	0.719	0.490	0.890	0.967	0.939	24.30	47.88	37.83
50% M: 50% T	0.10	0.50	0.34	0.824	0.973	0.859	1.095	1.126	1.113	30.35	46.30	36.65
25% M: 75% T	0.30	0.35	0.33	0.765	0.885	0.838	1.124	1.143	1.137	18.35	27.45	22.64
100% T	0.02	0.10	0.08	0.970	0.990	0.978	1.281	1.465	1.362	44.95	57.90	51.63

Figure S9. The scanning electron microscopy images for the following samples: **A.** 100% M, **B.** 75% M: 25% T, **C.** 50% M: 50% T, **D.** 25% M: 75% T, and **E.** 100% T. The scale bars are 500 nm.

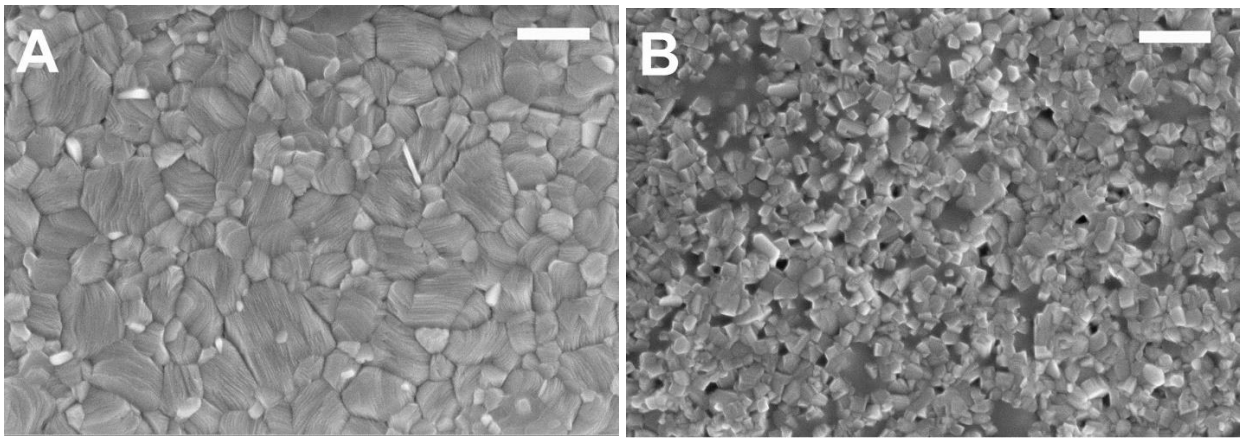

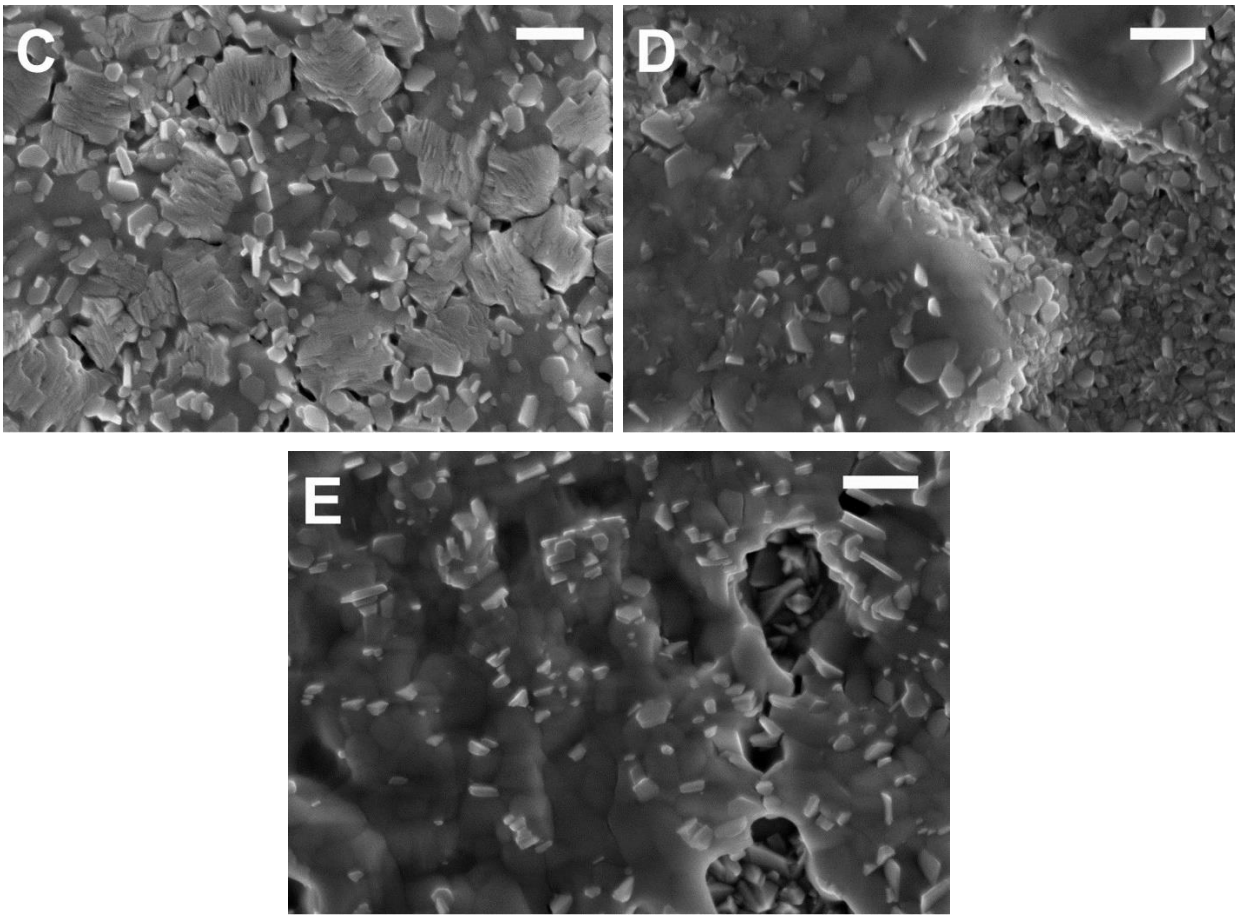

Figure S10. The W_{OC} for both phases of M-D alloys, M-I alloys, and M-T alloys. Phase 1 is based on bandgap from Tauc plot fitting at 525 nm absorptance onset, and phase 2 is based on bandgap at 825 nm absorptance onset.

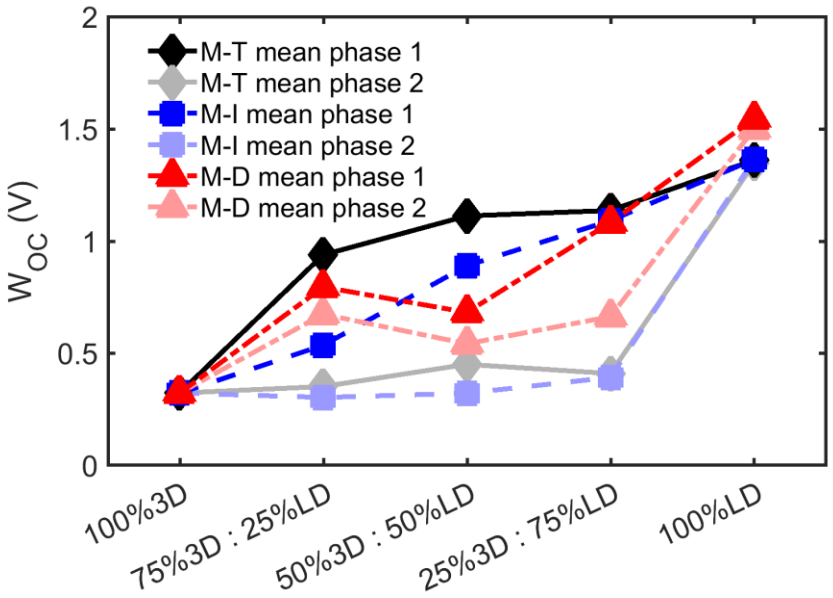

Figure S11. Change of photo-conductivity in TRMC as a function of time for **A.** 100% M **B.** 50% M: 50% T **C.** 25% M: 75% T **D.** 50% M: 50% D. All of these thin films are excited at 720 nm (excitonic peak).

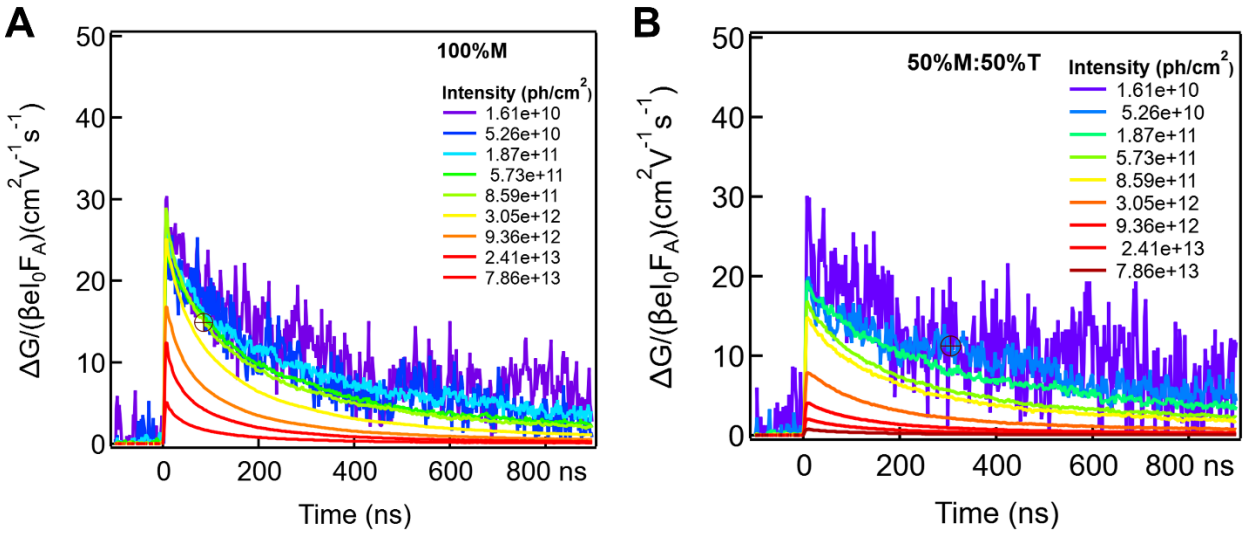

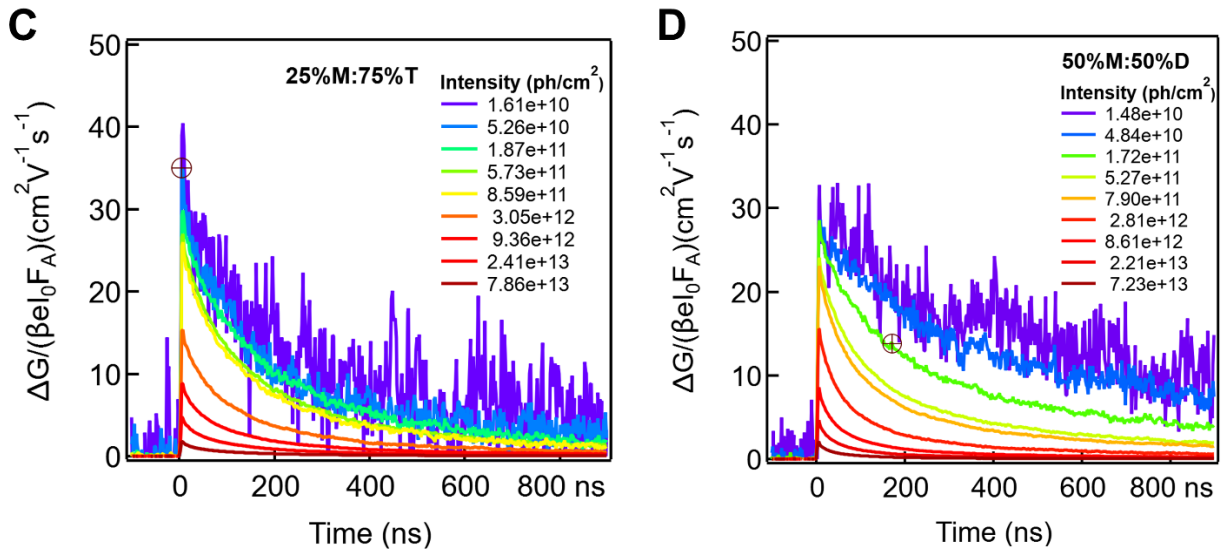

Figure S12. Change of photo-conductivity in TRMC as a function of time for **A.** 100% D **B.** 100% I **C.** 100% T. All of these thin films are excited at 490 nm (excitonic peak).

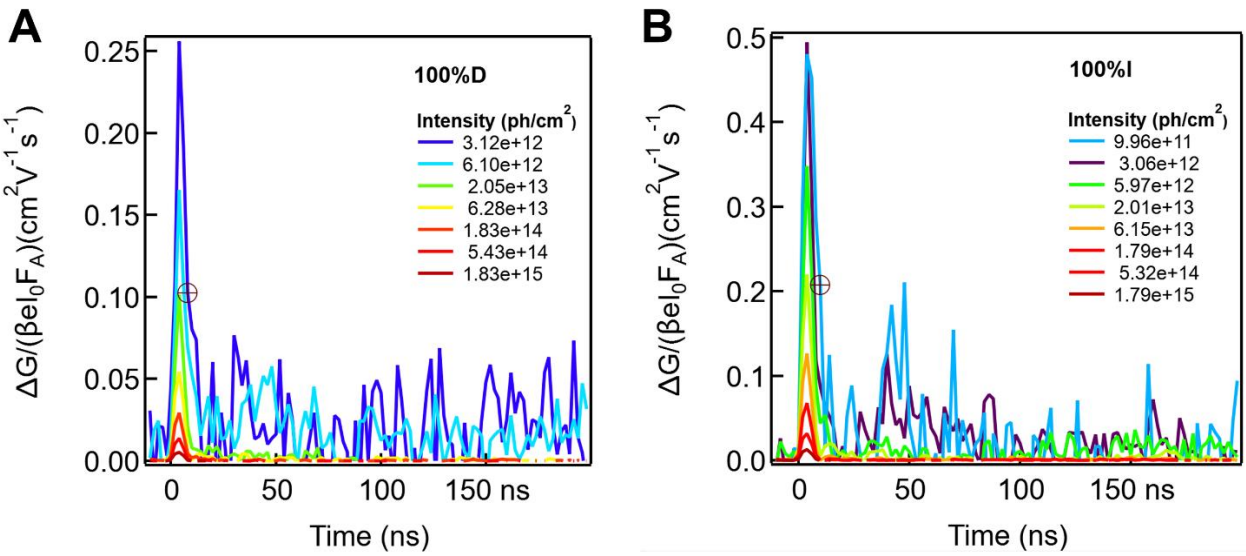

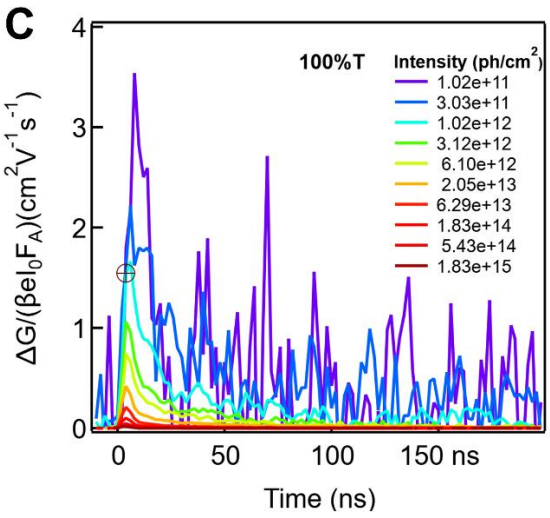

Figure S13. Half-lifetime of charge carriers based on TRMC measurement. Excited at the excitonic peaks (720 nm for 100% M, 75% M: 25% T, 50% M: 50% T, 25% M: 75% T, 50%M: 50% D, and 490 nm for 100% D, 100% T, and 100% I).

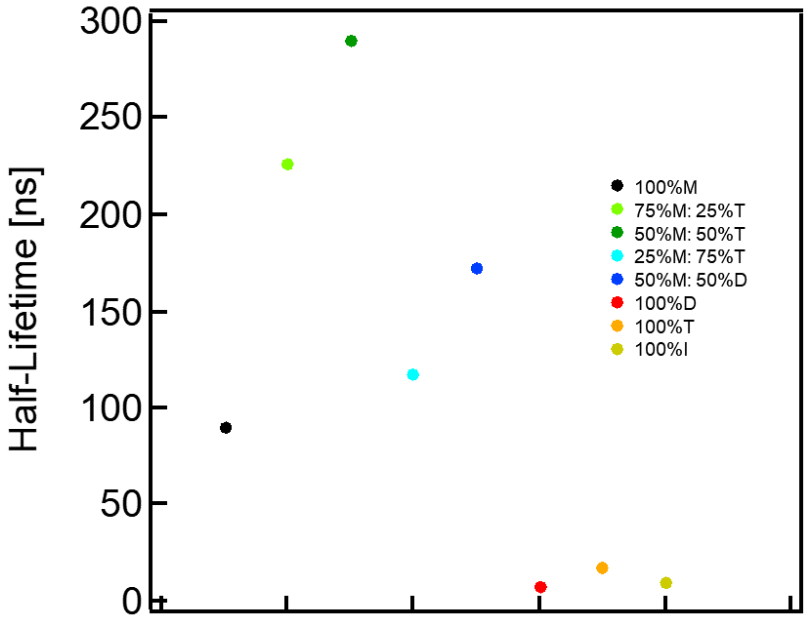

Figure S14. A. Maximum change of photo-conductivity in TRMC measurement. **B.** Half-lifetime of the charge carriers for LD perovskites, excited at 490 nm.

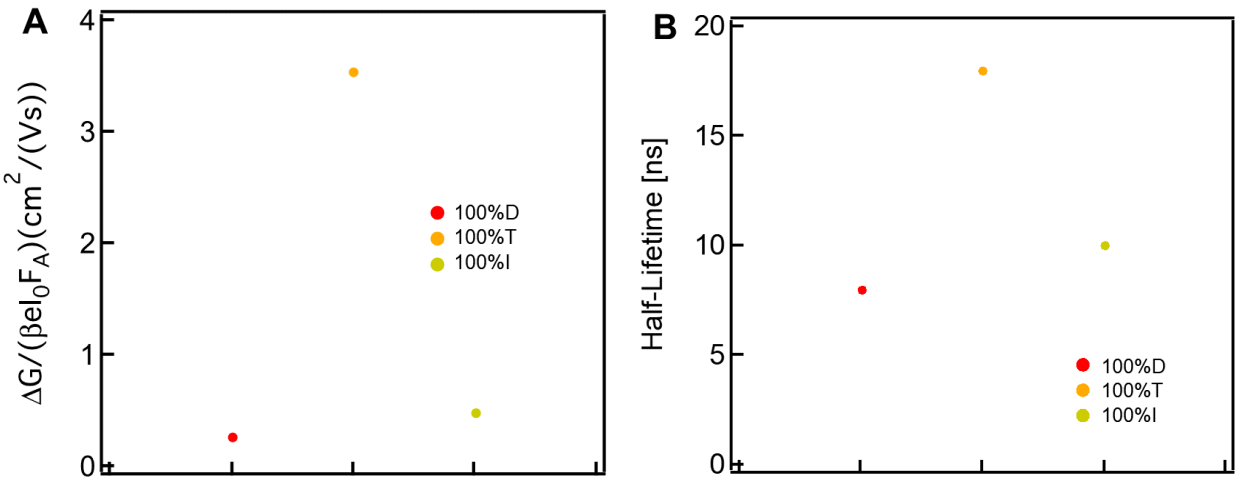

Figure S15. The absolute, average, PCE (power conversion efficiency) hysteresis, normalized for M-T, M-D, M-I alloys devices.

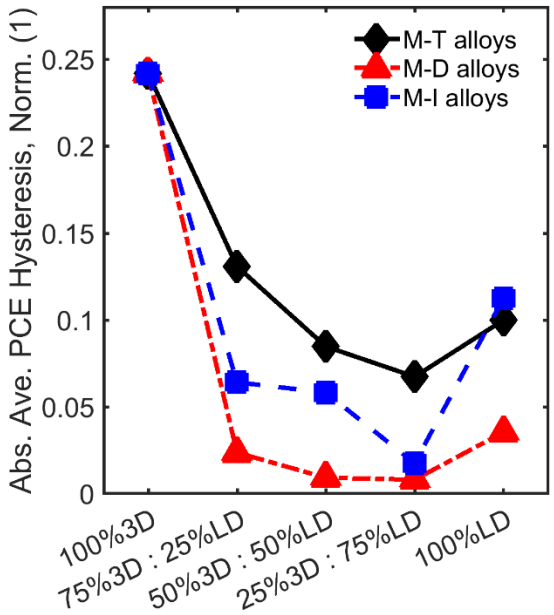

Figure S16. The change in $\Delta T/T_0$ of M-T alloys measured using THz pump-probe method. The decay slows down with increasing T concentration up to 75% T, and then decay increases again for 100% T sample.

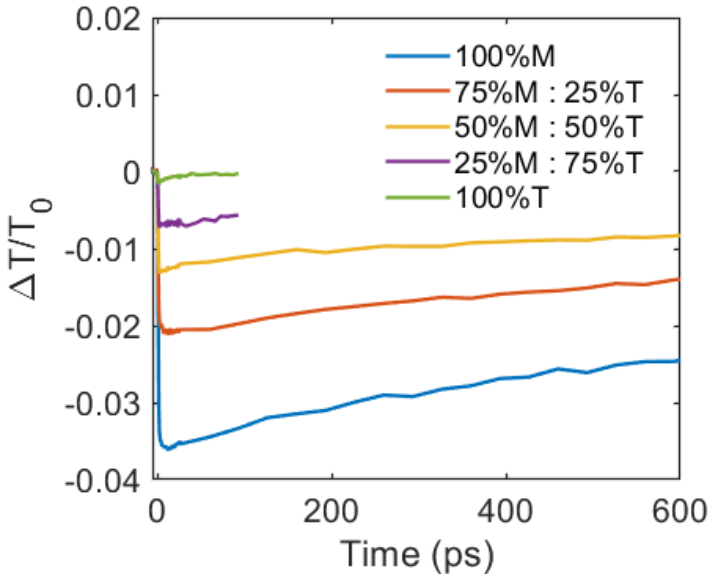

References

1. Wei F, Deng Z, Sun S, et al. The synthesis, structure and electronic properties of a lead-free hybrid inorganic–organic double perovskite (MA) $_2$ KBiCl $_6$ (MA = methylammonium). *Mater Horizons*. 2016;3(4):328-332. doi:10.1039/C6MH00053C
2. Sun S, Fang Y, Kieslich G, White TJ, Cheetham AK. Mechanical properties of organic–inorganic halide perovskites, CH $_3$ NH $_3$ PbX $_3$ (X = I, Br and Cl), by nanoindentation. *J Mater Chem A*. 2015;3(36):18450-18455. doi:10.1039/C5TA03331D
3. Mancini A, Quadrelli P, Amoroso G, et al. Synthesis, structural and optical characterization of APbX3 (A=methylammonium, dimethylammonium, trimethylammonium; X=I, Br, Cl) hybrid organic-inorganic materials. *J Solid State Chem*. 2016;240:55-60. doi:10.1016/j.jssc.2016.05.015